NJC

PAPER

View Article Online
View Journal | View Issue

Check for updates

Cite this: *New J. Chem.*, 2022, **46**, 1238

A phase transition-induced photocathodic p-$CuFeO_2$ nanocolumnar film by reactive ballistic deposition†

P. V. R. K. Ramacharyulu,[a] Yong Ho Lee,[b] Kenta Kawashima,[c] Duck Hyun Youn,[d] Jun-Hyuk Kim,[e] Bryan R. Wygant,[c] C. Buddie Mullins[c] and Chang Woo Kim*[ab]

In the present study, Cu–Fe–O vertical nanocolumnar structured arrays are deposited on fluorine-doped tin oxide substrates by the reactive ballistic deposition technique in an oxygen atmosphere by fixing the deposition angle at 85°. The scanning electron microscopy images show the presence of arrays of individual columns. The photocurrent density of the Cu–Fe–O sample annealed at 650 °C for 2 h in argon ($CuFeO_2$) is determined to be -0.22 mA cm^{-2} at 0.4 V *versus* RHE in 1 M NaOH under AM 1.5 G illumination, while the same annealed in air exhibits a photocurrent density of 0.12 mA cm^{-2} at 1.23 V *versus* RHE. Here, the film annealed in an argon atmosphere at 650 °C exhibits a p-type characteristic with cathodic photocurrent, while the film annealed in air depicts an n-type characteristic with anodic photocurrent. The switch in conductivity from n-type to p-type is induced by the phase transition from amorphous Cu–Fe–O to delafossite $CuFeO_2$. The generation of cathodic photocurrent from p-$CuFeO_2$ is also expected to be from the presence of the Cu^{2+}/Cu^{+} redox couple, which is evidenced by X-ray photoelectron spectroscopy.

Received 29th September 2021,
Accepted 2nd December 2021

DOI: 10.1039/d1nj04656j

rsc.li/njc

Introduction

Photoelectrochemical (PEC) water splitting is a promising approach for the production of renewable, clean, and sustainable solar fuel. The use of the solar fuel is an alternative for fossil fuel consumption, which would minimize the effects of the energy crisis and environmental pollution.[1–3] Employing semiconductors as photoelectrodes for PEC water splitting has been studied extensively after the breakthrough in 1972 which employed a TiO_2 semiconductor.[4–6] Identifying semiconductor materials with effective PEC performance that are also highly robust and easily fabricated has been a major challenge.[7] Based on the type of semiconductor, photoelectrodes can be classified as either n-type photoanodes, in which photoexcited holes are consumed in the water oxidation reaction, or p-type photocathodes, where the photo-generated electrons are used for the water reduction reaction. Metal oxide semiconductors are predominantly n-type materials as they form oxygen vacancies readily. Several common n-type photoanodes include ZnO,[8] WO_3,[9] Fe_2O_3,[10] $BiVO_4$,[11] and $ZnFe_2O_4$.[12] Conversely, there are only a few p-type semiconductor metal oxides,[13–15] as the generation of metal ion vacancies or oxygen interstitials which induces p-type conductivity is very difficult to achieve.[16,17] Accordingly, the progress in finding suitable p-type photocathode materials has been relatively slow due to the limited availability of appropriate candidate materials.

Various strategies have been employed to enhance the efficiency of photoelectrodes, including doping, constructing heterojunctions, and loading co-catalysts which might introduce new interfaces that act as recombination centers.[18–20] Interestingly, the conductivity type of a semiconductor can be switched by doping foreign impurities into it, which greatly brakes the limits of currently available materials.[21–25] A few studies report that phase transition takes place by doping metal ions into the lattice, enhancing the photoresponse and stability.[21–25] Another approach to achieve the transition from n-type to p-type is treating the sample in a reductive ambient atmosphere which changes the dominant carriers on the surface.[26] In this regard, the strategy of switching conductivity

---

[a] Department of Nanotechnology Engineering, College of Engineering, Pukyong National University, Busan, 48513, Republic of Korea. E-mail: kimcw@pknu.ac.kr
[b] Department of Smart and Green Technology Engineering, Pukyong National University, Busan 48513, Republic of Korea
[c] McKetta Department of Chemical Engineering, Department of Chemistry, Texas Materials Institute, Center for Electrochemistry, University of Texas at Austin, Austin, Texas 78712, USA
[d] Department of Chemical Engineering, Kangwon National University, Chuncheon, Gangwon-do 24341, Republic of Korea
[e] Korea Technology Finance Corporation (KOTEC), Busan, 48400, Republic of Korea

† Electronic supplementary information (ESI) available: Top-view and cross-sectional FESEM images, EDS elemental mapping analysis results, linear sweep voltammograms, and Raman spectra. See DOI: 10.1039/d1nj04656j

via phase transition could be used to alter the electrical properties of metal oxides.

One-dimensional (1D) semiconductor-based photoelectrodes have drawn attention over the past decade. Compared with bulk materials, 1D materials have exceptional advantages like high specific surface area and pore volume, effective photon absorption and scattering, less reflectivity, and fast and long-distance charge transport. These properties are expected to be beneficial for PEC water splitting. Specifically, the charge transfer phenomenon can be enhanced along the vectorial direction, which significantly promotes the separation of photo-generated charge carriers. Interestingly, the scattered light can be once again utilized in 1D nanostructured photoelectrodes. By designing the morphology and path length of the incident light, the light harvesting ability can be improved.[27,28] Additionally, due to less reflectivity, 1D vertical nanostructured materials absorb a large portion of sunlight. In connection with this, several systems have been studied and fabricated by the reactive ballistic deposition (RBD) technique providing photo-active and stable vertical nanostructured electrodes.[29–35]

RBD is a deposition technique for the preparation of both binary and ternary metal oxide films by using multiple evaporative sources or reactive gases and by varying the deposition angles and stoichiometry of the deposited elements. So far, various materials like TiO_2, ZnO, Fe_2O_3, MgF_2, and Pd have been prepared by using this method. In an early work, Dohnalek and co-workers used the RBD technique to deposit high surface area MgO films.[30] Inspired by the Pacific Northwest National Laboratory (PNNL), Mullins *et al.* also employed this technique to deposit TiO_2,[31] TiC,[32] α-Fe_2O_3,[33] Ti- and Sn-doped α-Fe_2O_3,[34] and $BiVO_4$.[35]

Various ternary oxides have been reported that have used widely abundant elements. Among these, delafossite ($CuFeO_2$) exhibits a band gap of 1.5 eV,[36] which is less than Cu_2O (2.0 eV),[37] due to the presence of the Cu 3d bands below the Fe 3d bands in its band structure. In connection with this, Jang *et al.* prepared a $CuFeO_2$ film on a fluorine-doped tin oxide (FTO) substrate by a solution-based technique which exhibited a photocurrent density of -0.3 mA cm^{-2} at 0.4 V *versus* the reversible hydrogen electrode (RHE).[37] However, upon conventional thermal annealing in air atmosphere for a prolonged time, the photocurrent density doubled for a bare $CuFeO_2$ photocathode (-0.62 mA cm^{-2} at 0.4 V *versus* RHE).[37] By using hybrid microwave annealing, the photocurrent density was further enhanced by intercalating extra oxygen into $CuFeO_2$, in combination with the modification of a NiFe-layered double hydroxide (NiFe LDH)/reduced graphene oxide (RGO) electrocatalyst.[37]

In an attempt to enhance the photoresponse by phase transition, here we have deposited a 1D Cu–Fe–O nanocolumnar structure on an FTO substrate using the RBD technique, followed by annealing in air or an argon atmosphere. The as-prepared films were then annealed to attain crystallinity. The annealed films were characterized by microscopic and spectroscopic techniques; their PEC properties were studied. The transition between the two different conductivity types for the photoelectrodes was identified *via* PEC photocurrent measurements. Thus, the sample containing p-$CuFeO_2$ exhibited a cathodic photocurrent, which is a characteristic of p-type semiconductors. The cathodic photocurrent of p-$CuFeO_2$ is expected to be from the presence of the Cu^+/Cu^{2+} redox couple.

Results

Cu–Fe–O nanowire arrays were synthesized using the RBD technique with a metal (Cu and Fe) evaporative deposition angle of ~85°. Specifically, we carried out as the co-deposition of iron and copper with an FTO substrate held at ambient temperature. The advantage of high glancing angle deposition is that it generates highly porous nanocolumnar structures with potentially efficient photocurrent response, easier electron/hole transport to the electrolyte due to more optimal feature size, and high interfacial area. As per earlier reports, films deposited at higher glancing angles exhibited higher photocurrents than the samples deposited at lower angles.[31–35] It is expected that the films synthesized through the RBD offer large areas of interface between the film and electrolyte and concurrently shorten the transport distance for the originated minority carriers in the bulk to reach the electrolyte, thus improving the (PEC) performance of the electrodes.[29]

The FTO substrates were cleaned rigorously before deposition. Fig. 1(a) shows a schematic representation for the growth of the Cu–Fe–O nanowires on the as-cleaned FTO substrate by the RBD. By keeping the glancing angle at 85°, Cu and Fe metals were evaporatively co-deposited on the FTO substrate in an oxygen atmosphere at ambient temperature. After the deposition, the formation of an amorphous Cu–Fe–O vertical columnar structure can be seen in Fig. 1(b). The crystalline Cu–Fe–O was achieved by the heat treatment of amorphous samples (Fig. 1(c)).

Field emission scanning electron microscopy (FESEM) studies were carried out to evaluate the morphological evolution of the as-deposited and heat-treated samples. Fig. 2(a) and (b) show the top-view images of the vertically aligned large-scale aggregates of the as-deposited Fe–O columns and Cu–Fe–O columns, respectively.

The cross-sectional images depict the uniform deposition of the respective layers on the substrate successfully. Energy dispersive X-ray spectroscopy (EDS) analysis confirms the presence of Fe in Fe–O, Fe, and Cu elements with obvious

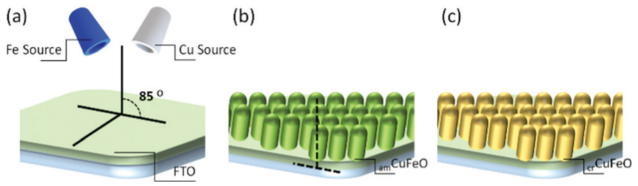

Fig. 1 Schematic illustration of ballistic deposition of the Cu–Fe–O nanowire film on an FTO substrate. (a) Deposition of Fe and Cu sources with an 85° angle. (b) The as-deposited nanowire arrays with amorphous and (c) crystalline phases after heat treatment.

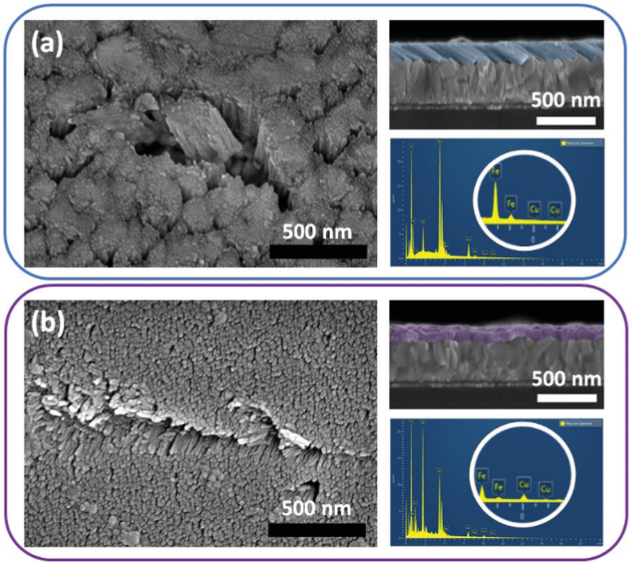

Fig. 2 Typical top-view and cross-sectional FESEM images and EDS elemental analysis results of the as-deposited (a) Fe–O nanocolumn arrays and (b) Cu–Fe–O nanocolumn arrays.

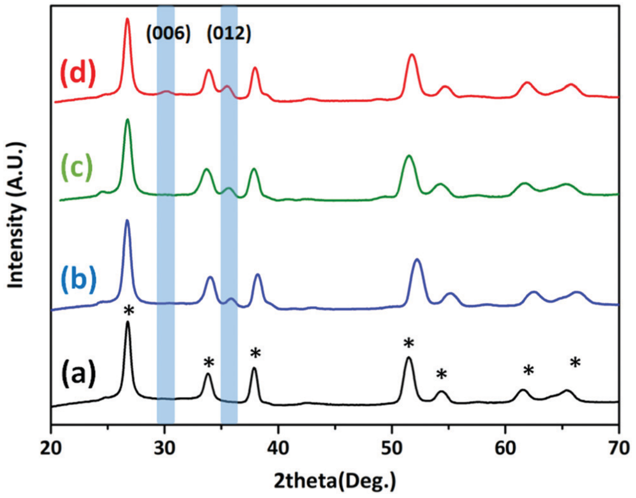

Fig. 3 Comparison of XRD patterns of (a) the as-deposited sample and the samples heat-treated at (b) 450, (c) 550, and (d) 650 °C for 2 h under Ar flow. The (006) and (012) diffraction peaks correspond to delafossite ($CuFeO_2$) and the diffraction peaks denoted with * correspond to the FTO substrate.

amounts in the Cu–Fe–O sample. Fig. S1 (ESI†) shows the magnified top-view images of Fe–O and Cu–Fe–O on FTO substrates which clearly depict the surfaces of the individual nanocolumns in both cases. Interestingly, it is observed that individual nanocolumns in the Cu–Fe–O is well-ordered with homogeneity as compared to those of the Fe–O. The magnified cross-sectional view of both the Fe–O and Cu–Fe–O nanocolumns can be seen in Fig. S2 (ESI†). The images confirm that the films consist of an array of separated filaments, and it is difficult to depict the exact growth angle of the columns in connection with the surface. It is also clear that the growth angle is less than the incident vapor deposition angle of 85°. The top-view EDS elemental mapping images of the as-deposited Fe–O columns confirm the presence of Fe, O, Si, and Sn elements which can be seen in Fig. S3 (ESI†). It can be clearly observed that there are no peaks related to Cu in the EDS spectrum, which indicates that it is a pure Fe–O phase. The cross-sectional EDS elemental mapping images of as-deposited Cu–Fe–O nanocolumns depict the uniform elemental distribution and confirm the presence of Cu, Fe, O, Si, and Sn elements, which can be seen in Fig. S4 (ESI†). The ratio of Cu to Fe was found to be 2.03 : 1.

The as-deposited films were annealed at 450, 550, and 650 °C to transform the amorphous copper iron oxides into crystalline samples. X-ray diffraction (XRD) measurements were employed to determine the phase and crystallinity of the as-deposited Cu–Fe–O nanocolumnar films heated at three consecutive temperatures of 450, 550, and 650 °C in an argon atmosphere, which can be seen in Fig. 3. The as-deposited films exhibited SnO_2 (JCPDS No. 46-1088) diffraction peaks (indexed by * in XRD) which arise from the FTO substrate and the absence of other peaks, indicating that the films are amorphous prior to annealing, as shown in the schematic illustration (Fig. 1(b)). When the sample was annealed at 450 °C in an argon atmosphere, a difraction peak was observed at around 36° in the XRD pattern; this peak could be ascribed to the presence of the iron-based oxide. When the annealed temperature increased to 550 °C, no change in the XRD pattern was observed. The peak that appeared at 36° was predicted to be from the (111) planes of FeO[38] and the (012) planes of Cu–Fe–O.[37] Fe–O is a nonstoichiometric oxide and is prone to oxidation to other iron oxide materials at elevated temperatures.[38] With an increase in annealing temperature upto 650 °C, a new diffraction peak observed at around 30° was attributed to the (006) diffraction along with the (012) diffraction of $CuFeO_2$ indicating the complete formation of delafossite $CuFeO_2$. This observation indicates that low-temperature annealing is not sufficient to obtain a pure delafossite phase and is consistent with earlier reports.[37] The alteration in the composition of the film shows the complete formation of typical delafossite $CuFeO_2$ (JCPDS No. 25-2146) as the single phase in the annealed films at 650 °C in an argon atmosphere with a preferred orientation along the (012) plane.[36,37] In order to confirm the formation of the delafossite phase, further characterization studies were performed which are discussed in a later part. It was also reported that phase transition is more obvious in the film than in the powder case due to the additional strain in the crystal structure of the film.[37] The film annealed at 650 °C in argon is transparent brown in colour indicating the absence of copper oxide, iron oxide, and copper ferrite. This result is in accordance with earlier reports regarding $CuFeO_2$.[36,39,40] Crystallinity aids in improving the electron transport vertically through the film due to the higher conductivity of this plane relative to other samples.[34] XRD analysis confirms that copper does not exist as solid copper or copper oxide.

Fig. 4(a) shows the FESEM image of the Cu–Fe–O nanowire array after heat treatment at 650 °C for 2 h which depicts the

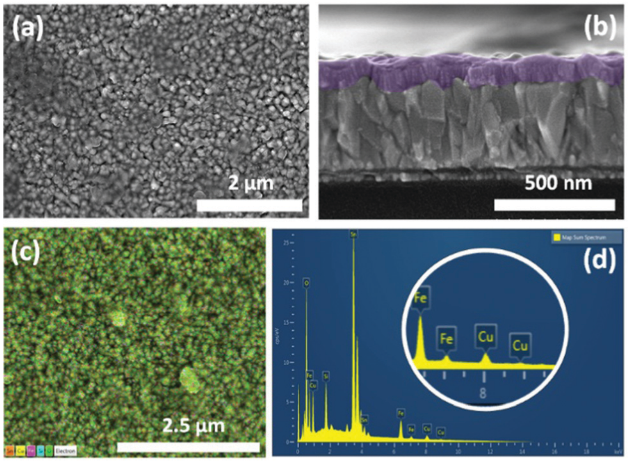

Fig. 4 Typical (a) top-view and (b) cross-sectional FESEM images, (c) top-view elemental mapping image, and (d) EDS spectrum of the Cu–Fe–O nanowire arrays heat-treated at 650 °C for 2 h under Ar flow.

highly uniform and densely packed structure throughout the film with a spherical and sharp needle-like morphology. Fig. 4(b) shows the cross-sectional FESEM image of the Cu–Fe–O nanowire array deposited throughout the film which is in good contact with the FTO substrate. Fig. 4(c) and (d) show the top-view EDS elemental mapping and EDS spectrum of the Cu–Fe–O nanowire arrays which depict the presence of Fe, Cu, Sn, and O elements. Fig. S5 and S6 (ESI†) show the magnified top-view and cross-sectional images of the heat-treated Cu–Fe–O nanowire arrays. Fig. S7 (ESI†) shows the top-view EDS elemental mapping images of the heat-treated Cu–Fe–O sample which confirms the presence of Cu, Fe, O, Si, and Sn elements, and the ratio of Cu to Fe was found to be 1.2 : 1. The EDS spectrum of Fe and Cu is highlighted in both cases to show the presence of Cu in the Cu–Fe–O. The difference in the ratio of Cu to Fe from the cross-section and top-view could result from the formation of metallic impurities which could not be detected by XRD.

X-ray photoelectron spectroscopy (XPS) analysis was performed to detect the change in the electronic states of Cu, Fe, and O elements within the sample. Fig. 5(a) shows the full survey spectrum which depicts the presence of Cu, Fe, O, and C on the sample surface, indicating the formation of oxides of copper and iron, which is consistent with the EDS results. The high-resolution spectra corresponding to Cu, Fe, and O are shown in Fig. 5(b–d). The doublet peaks located at 932.9 and 952.6 eV can be ascribed to the Cu $2p_{3/2}$ and Cu $2p_{1/2}$ spin–orbit components of monovalent copper Cu^+,[41] and the other set of doublet peaks at 934.9 and 954.7 eV corresponds to divalent copper Cu^{2+}, formed due to the easy oxidation of Cu in the humid air.[37] No peaks were detected in the range of 933–934 eV which indicates the absence of lattice-bound Cu^{2+} species.[42–44] The peaks representing Cu^{2+}, and the two satellite peaks of Cu $2p_{3/2}$ and Cu $2p_{1/2}$, appear at 942 and 962 eV, due to an unfilled $3d^9$ shell of Cu^{2+}.[45] The same observation is consistent with earlier reports. The Fe 2p XPS spectrum shows well-resolved signals at 711.2 and 724.8 eV which correspond to the +3 oxidation state of iron in Fe_2O_3.[46] However, the less intense other resolved signals at 709.9 and 723.8 eV correspond to the +2 oxidation state of iron.[47] The O 1s XPS spectrum shows three peaks at 530.8, 532.1, and 532.7 eV corresponding to the lattice oxygen, oxygen vacancies, and adsorbed hydroxyl groups on the surface, respectively. From an earlier study by Dupin *et al.*, the peak at lower binding energy (BE) is allocated to O^{2-} ions, the peak at middle BE is ascribed to O^- ions, and the peak at higher BE is attributed to chemically adsorbed oxygen (O_{Chem}), on the surface.[48,49] This result indicates the presence of Cu^+/Cu^{2+} on the surface of the sample. This confirms the formation of the $CuFeO_2$ delafossite phase, which is consistent with the XRD result.

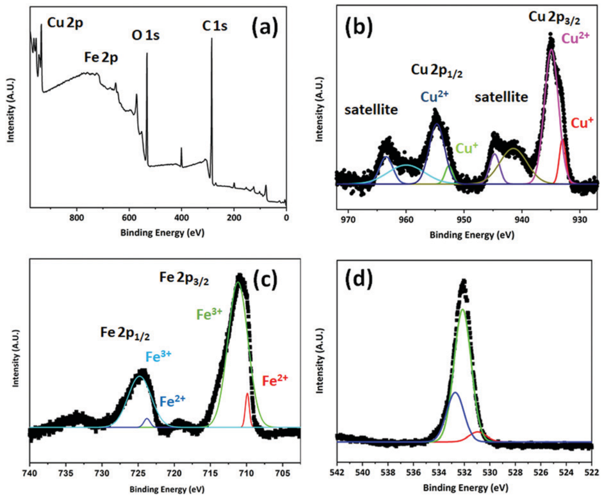

Fig. 5 XPS profiles of the Cu–Fe–O nanowire sample heat-treated at 650 °C for 2 h under Ar flow: (a) survey spectrum and high-resolution spectra of (b) Cu 2p, (c) Fe 2p, and (d) O 1s.

Fig. 6(a) reveals the ultraviolet and visible (UV-vis) spectra of the Cu–Fe–O nanowire arrays heated at the three consecutive temperatures of 450, 550, and 650 °C for 2 h. All the samples show broad absorption in the visible light region. The sample annealed at 450 °C is black in colour and shows two peaks at 450 and 550 nm attributed to the direct charge transfer and indirect transition in Fe-based oxides, respectively.[33] By increasing the annealing temperature from 450 to 550 °C, an apparent blueshift has occurred with an increase in the absorbance; however, on further increasing the temperature from 550 to 650 °C, the absorbance further increased.

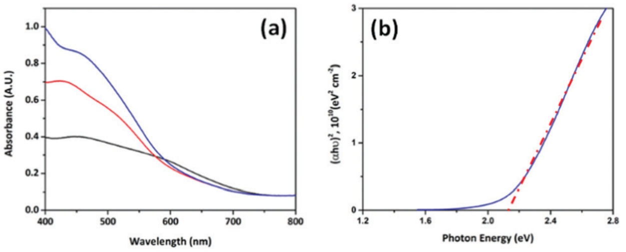

Fig. 6 (a) UV-vis absorption spectra of the Cu–Fe–O nanowire samples heat-treated at 450 (black), 550 (red), and 650 °C (blue) for 2 h under Ar flow. (b) Tauc plot of the Cu–Fe–O sample heat-treated at 650 °C for 2 h under Ar flow.

The valence band of $CuFeO_2$ consists of Cu 3d and O 2p orbitals, while the conduction band contains Fe 3d orbitals.[40] The $CuFeO_2$ samples exhibit direct charge transfer from the O 2p valence band to the Fe 3d conduction band and indirect d–d transition. With an increase in the annealing temperature, there is a significant difference in the light absorption properties. Fig. 6(b) shows the direct band gap of the $CuFeO_2$ film prepared by the RBD followed by annealing at 650 °C. The optical band gap of the crystalline semiconductor is calculated using the equation $(\alpha h\nu)^n = A(h\nu - E_g)$, where α, h, ν, E_g, and A are light absorption coefficient, the Planck constant, frequency, band gap, and a constant, respectively. Here, the n value of the direct and indirect transition is 2 and 1/2, respectively. The band gap value of the Cu–Fe–O annealed at 650 °C can be estimated from the absorbance spectra by using a Tauc plot, and the band gap is approximately 2.1 eV. The absorption spectrum of the sample annealed at 650 °C for 2 h corresponding to the formation of $CuFeO_2$ is consistent with earlier reports.[37] As per earlier reports, $CuFeO_2$ exhibits three types of band gaps: 1.47 (indirect band gap), 3.1 (direct transition), and 2.1 eV (either direct or indirect).[50–53]

Fig. S8 (ESI†) displays the *J–V* curve for the Cu–Fe–O nanowire array sample annealed at 450 °C for 1 h in argon which shows the anodic photocurrent with an increase in the positive potential depicting the properties of an n-type semiconductor.

Fig. 7(a) shows the *J–V* curves for the Cu–Fe–O samples annealed at 550 °C for 1, 1.5, and 2 h illustrating that there is an increase in cathodic photocurrent with an increase in annealing time. Interestingly, when the annealing temperature is increased to 650 °C, a switch in the conductivity happens from n-type to p-type. This phenomenon is ascribed to the phase transition-induced formation of delafossite from iron oxide. Fig. 7(b) shows that the Cu–Fe–O samples annealed at 650 °C for 1, 1.5, and 2 h in an argon atmosphere demonstrated that cathodic photocurrent increases with the cathodically increasing applied potential indicating the properties of a p-type semiconductor. The samples annealed at 650 °C for 1, 1.5, and 2 h exhibited the photocurrent density values of −0.18, −0.19, and $-0.22\ \mathrm{mA\ cm^{-2}}$ at 0.4 V *versus* RHE, respectively. This confirms that with an increase in heat treatment, the cathodic current increases due to the formation of $CuFeO_2$. Fig. 7(c) shows the photocurrent density *versus* time (*J–t*) curves of the Cu–Fe–O nanowire arrays annealed at 650 °C for 1.5 and 2 h in argon. The two photocathodes display a relatively steady value during the thirty-minute test at an applied potential of 0.4 V *versus* RHE. In Fig. 7(c), it is clear that the sample annealed for 2 h has the highest photocurrent density of $-0.22\ \mathrm{mA\ cm^{-2}}$. The negative current spikes upon turning off the light signify the accumulation of electrons at the semiconductor/liquid interface (*i.e.*, trap sites), and simultaneously, the positive spikes represent the back reaction of the release of electrons from the trap sites.[54] The sample annealed for 1.5 h showed a positive spike after 28 min. However, there is no positive spike in the sample annealed for 2 h indicating the suppression of recombination of photogenerated charge carriers.

In order to confirm the switch in conductivity, the iron oxide and copper iron oxide were annealed in air. Fig. S9 (ESI†) shows the linear sweep voltammetry (LSV) and *J–V* curves of the deposited Fe–O and Cu–Fe–O annealed at 650 °C for 2 h in air. The PEC performance of iron oxide and copper iron oxide annealed in air exhibits an anodic photocurrent consistent with the properties of an n-type semiconductor. With an increase in positive potential, the anodic photocurrent density increases and exhibited a value of $0.3\ \mathrm{mA\ cm^{-2}}$ at 1.23 V *versus* RHE for

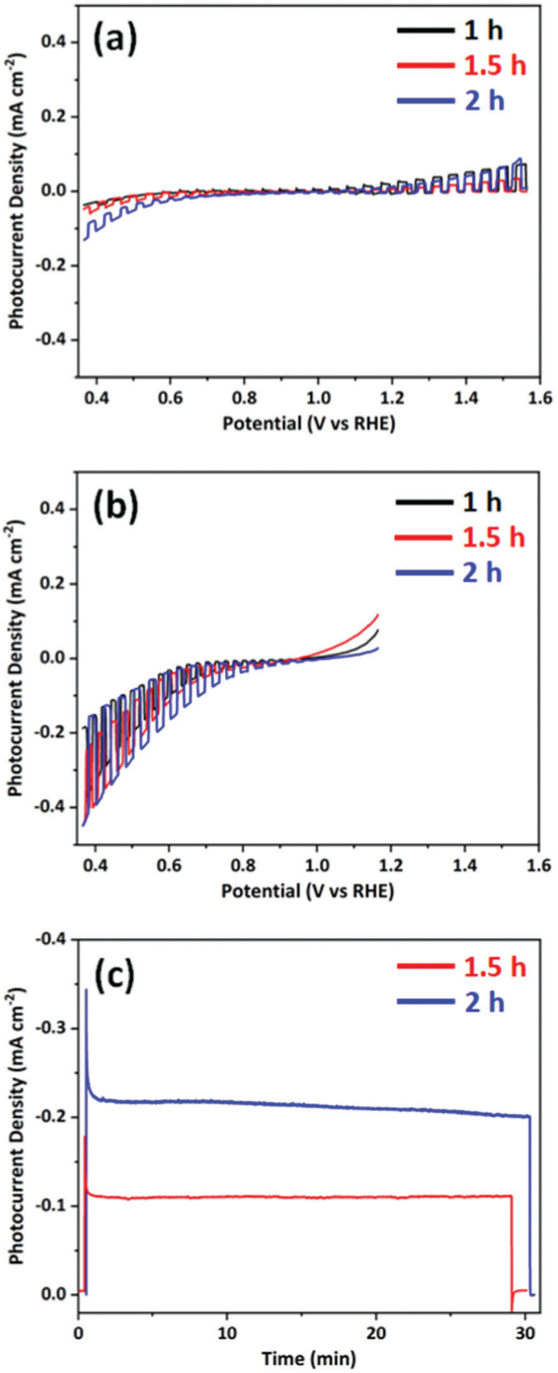

Fig. 7 *J–V* curves of the Cu–Fe–O nanowire arrays heat-treated at (a) 550 and (b) 650 °C for 1 (black), 1.5 (red), and 2 h (blue) under Ar flow. (c) *J–t* curves of the samples heat-treated at 650 °C for 1.5 (red) and 2 h (blue) under Ar flow. All the *J–t* curves were recorded at 0.4 V *versus* RHE.

iron oxide, which can be seen in Fig. S9(a) (ESI†). On the other hand, copper iron oxide showed a less anodic photocurrent of 0.12 mA cm^{-2} at 1.23 V *versus* RHE over the same potential region, as seen in Fig. S9(b) (ESI†). The Fe–O and Cu–Fe–O samples annealed in air for 2 h depict the properties of an n-type semiconductor. When Cu was introduced into the host lattice of FeO, a substantial decrease in anodic photocurrent was observed. This phenomenon is ascribed to the charge recombination effect of the host Fe_2O_3 at high concentrations of the dopant.[55,56] In hematite, copper monovalent/divalent ions typically introduce positive charge carriers. Thus, the anodic photocurrent density decreases upon the introduction of Cu into the Fe_2O_3 lattice.[57] Fig. S10 (ESI†) shows the Raman spectra of the as-deposited and heat-treated Cu–Fe–O samples. For the as-deposited sample, four Raman vibration active modes were clearly observed at 215, 282, 397, and 615 cm^{-1}, which may be assigned to A_{1g}, E_g, E_g, and E_g of Fe_2O_3, respectively.[58] Here, the broad peak at 1295 cm^{-1} may correspond to two-magnon Raman scattering.[58,59] On the other hand, the Cu–Fe–O sample heat-treated at 650 °C for 2 h did not show any peaks related to Fe–O and exhibited a significantly weak peak at 670 cm^{-1} which is attributed to the A_{1g} Raman active mode of delafossite.[60] This may be attributed to the structural evolution of $CuFeO_2$ through the annealing process under an argon atmosphere, as shown in the XRD. The sample annealed at 650 °C for 2 h did not contain any Fe–O related peaks, which indicates the complete transformation of the structure.

When the Cu–Fe–O sample is annealed in a reductive ambient atmosphere, it limits the oxygen molecules and creates more oxygen vacancies inside the Cu–Fe–O lattice by removing oxygen anions, thus contributing to the p-type conductivity. The switch in conductivity is not from Sn doping, as the FTO is stable up to 800 °C.[61] Fig. 7 and Fig. S9 (ESI†) confirm the phase transformation from n-type to p-type.

High crystallinity with reduced defects in a photoelectrocatalyst is highly beneficial for facile charge transfer. However, annealing at 650 °C in an argon atmosphere induces a phase transition, which exhibits the p-type semiconductor properties of $CuFeO_2$ and shows the onset of cathodic current generation with a value of −0.22 mA cm^{-2} at 0.4 V *versus* RHE. The cathodic photocurrent proves that the $CuFeO_2$ photoelectrode exhibited p-type conductivity and could possibly be utilized as a photocathode for hydrogen evolution. These results are consistent with the XRD and XPS data. The particle aggregation also weakens the PEC performance with reduced surface area. Our as-suggested nanowire arrays can hardly be affected by such a negative effect of particle aggregation on PEC activity. These results indicate that phase transition induced p-$CuFeO_2$ is the active phase for the photoreduction of water and the most active form obtained by annealing at 650 °C. In addition to this, the enhancement in PEC performance could also be from the electrodes synthesized by the RBD which offer large areas of interface between the film and electrolyte, thus shortening the transport distance for minority carriers in the bulk to reach the electrolyte.

Conclusions

In conclusion, Cu–Fe–O nanowire arrays on FTO substrates were fabricated *via* the RBD process in which the evaporative co-deposition of Fe and Cu happened in ambient oxygen at the fixed deposition angle. Deposition at high glancing angles creates highly porous, columnar structures with high photocurrent response. The as-deposited Cu–Fe–O films were annealed to induce crystallinity. The as-deposited Cu–Fe–O films annealed in an argon atmosphere at low temperatures (450 and 550 °C) exhibited anodic photocurrents, which is characteristic of an n-type semiconductor. However, the Cu–Fe–O film annealed at a higher temperature (650 °C) in argon exhibited a cathodic photocurrent which is a property of the p-type semiconductor delafossite ($CuFeO_2$). The characterization results confirmed the crystalline nanocolumnar structures and uniform presence of the respective elements (Cu, Fe, and O) accompanied by visible light absorption. The films annealed at high temperatures for a prolonged time showed a switch in conductivity from n-type to p-type. The complete formation of delafossite showed the properties of a p-type semiconductor. Notably, the film annealed at 650 °C for 2 h in argon showed a cathodic photocurrent of −0.22 mA cm^{-2} at 0.4 V *versus* RHE in 1 M NaOH.

Experimental

Deposition of $CuFeO_2$ nanocolumnar films

$CuFeO_2$ nanocolumnar films were deposited onto fluorine-doped tin oxide (FTO) coated glass substrates (Pilkington, TEC15) in a high vacuum chamber equipped with two electron beam evaporators (Omicron, EFM 3s), an *x*–*y*–*z* sample manipulator mounted on a rotary seal, and a quartz crystal microbalance (QCM) and controller (Maxtek Inc.). After the 1.5 × 2 cm FTO-coated glass was cleaned and sonicated in ethanol and rinsed with demineralized water, it was loaded into the chamber. Cu and Fe rods (ESPI, 3 N purity) in a molybdenum crucible were loaded into each evaporator, which was directed at the FTO substrate. A deposition angle of 85° off-normal was used and then, the vacuum chamber was pumped down below 5×10^{-8} Torr. The chamber was backfilled with oxygen (Matheson, UHP grade) to approximately 6×10^{-6} Torr. The QCM-measured deposition rate and the deposition angle were used to determine the atomic flux of each component and the deposition time required for the target film thickness with a 0.3 rate (Å s^{-1}) of each metal. The deposition was performed at the ambient temperature of the chamber. The as-deposited films were heat-treated in argon and air at temperatures ranging from 450 to 650 °C for 1–2 h at a ramp rate of 10 °C min^{-1} in a tube furnace (Neytech), respectively.

Characterization

Morphological and film thickness characterization was performed using a ultra-high resolution (UHR) field emission scanning electron microscope (FESEM) (SU8230, Hitachi) with an energy dispersive X-ray spectroscopy (EDS) detector in the

National NanoFab Center. X-ray diffraction (XRD) patterns were obtained with a Rigaku Raxis Spider diffractometer employing Cu Kα radiation (the X-ray diffraction lab in the University of Texas at Austin). UV-vis transmission spectra were recorded with a V-670 (JASCO) spectrophotometer using a blank substrate as a baseline standard. X-ray photoelectron spectroscopy (XPS) surface analysis was performed using a MultiLab 2000 (THERMO VG SCIENTIFIC) X-ray photoelectron spectrometer. The adventitious carbon located at 284.8 eV was used to calibrate the samples. Raman spectra were recorded with a NRS-5100 (JASCO) spectrometer in the Pukyong National University Center for research facilities.

The photoelectrochemical test was carried out using a PL-9 (KST-P1) potentiostat coupled to a solar simulator (Newport, 300 W Xe source) with an AM 1.5 G filter (Asahi HAL-320, 100 mW cm^{-2}) in the Korea Center for Artificial Photosynthesis. For the PEC measurement, the power density of the incident light was adjusted to 100 mW cm^{-2} using an NREL certified reference cell (Photo Emission Tech., Inc.). In a typical experiment, a three-electrode cell composed of the prepared electrode (working electrode), an Ag/AgCl (in saturated KCl) electrode (reference electrode), a Pt wire (counter electrode), and 1 M NaOH (electrolyte) was used. Linear sweep voltammetry (LSV) curves were recorded at a scan rate of 25 mV s^{-1}. All the PEC measurements were performed using an Ag/AgCl reference electrode at room temperature, and the applied bias was converted to the RHE using the following Nernst equation:

$$E_{\mathrm{RHE}} = E_{\mathrm{Ag/AgCl}} + E^{\mathrm{o}}_{\mathrm{Ag/AgCl}} + 0.0591\ \mathrm{V} \times \mathrm{pH}$$

$$(E^{\mathrm{o}}_{\mathrm{Ag/AgCl}} = 0.1976\ \mathrm{V\ at\ 25\ ^{\circ}C}).$$

Author contributions

The manuscript was written through contributions from all the authors. All the authors approved the final version of the manuscript.

Conflicts of interest

There are no conflicts to declare.

Acknowledgements

This research was supported by the Basic Science Research Program through the National Research Foundation of Korea (NRF) funded by the Ministry of Education (2020R1I1A3072987) and the Korean government (MSIT) (2017R1D1A1B03033094). C.B.M. gratefully acknowledges the generous support of the Welch Foundation *via* grant F-1436.

Notes and references

1 K. Ohashi, J. McCann and J. O'M. Bockris, *Nature*, 1977, **266**, 610.

2 R. Van de Krol, Y. Q. Liang and J. Schoonman, *J. Mater. Chem.*, 2008, **18**, 2311–2320.

3 T. Hisatomi and K. Domen, *Nat. Catal.*, 2019, **2**, 387–399.

4 A. Fujishima and K. Honda, *Nature*, 1972, **238**, 37–38.

5 J. Cena, Q. Wu, M. Liu and A. Orlova, *Green Energy Environ.*, 2017, **2**, 100.

6 I. Concina, Z. H. Ibupoto and A. Vomiero, *Adv. Energy Mater.*, 2017, **7**, 1700706.

7 C. Jiang, S. J. A. Moniz, A. Wang, T. Zhang and J. Tang, *Chem. Soc. Rev.*, 2017, **46**, 4645.

8 X. Long, C. Wang, S. Wei, T. Wang, J. Jin and J. Ma, *ACS Appl. Mater. Interfaces*, 2020, **12**, 2452.

9 Y. Zhao, G. Brocks, H. Genuit, R. Lavrijsen, M. A. Verheijen and A. Bieberle-Hutter, *Adv. Energy Mater.*, 2019, **9**, 1900940.

10 F. Li, J. Li, F. Li, L. Gao, X. Long, Y. Hu and J. Ma, *J. Mater. Chem. A*, 2018, **6**, 13412.

11 L. Gao, F. Li, H. Hu, X. Long, N. Xu, Y. Hu and J. Jin, *ChemSusChem*, 2018, **11**, 2502.

12 J. H. Kim, Y. J. Jang, J. H. Kim, J.-W. Jang, S. H. Choi and J. S. Lee, *Nanoscale*, 2015, **7**, 19144.

13 A. Paracchino, V. Laporte, K. Sivula, M. Gratzel and E. Thimsen, *Nat. Mater.*, 2011, **10**, 456.

14 K. Sekizawa, T. Nonaka, T. Arai and T. Morikawa, *ACS Appl. Mater. Interfaces*, 2014, **6**, 10969.

15 S. Ida, K. Yamada, T. Matsunaga, H. Hagiwara, Y. Matsumoto and T. Ishihara, *J. Am. Chem. Soc.*, 2010, **132**, 17343.

16 K. Zhang, M. Ma, P. Li, D. H. Wang and J. H. Park, *Adv. Energy Mater.*, 2016, **6**, 1600602.

17 A. Liu, H. Zhu and Y.-Y. Noh, *Mater. Sci. Eng., R*, 2019, **135**, 85.

18 Y. J. Jang and J. S. Lee, *ChemSusChem*, 2019, **12**, 1835.

19 T. Hisatomi, J. Kubota and K. Domen, *Chem. Soc. Rev.*, 2014, **43**, 7520.

20 C. M. Ding, J. Y. Shi, Z. L. Wang and C. Li, *ACS Catal.*, 2017, **7**, 675.

21 W. Liu, F. X. Xiu, K. Sun, Y. H. Xie, K. L. Wang, Y. Wang, J. Zou, Z. Yang and J. L. Liu, *J. Am. Chem. Soc.*, 2010, **132**, 2498.

22 W. B. Ingler Jr, J. P. Baltrus and S. U. M. Khan, *J. Am. Chem. Soc.*, 2004, **126**, 10238.

23 J. Kamimura, P. Bogdanoff, M. Ramsteiner, P. Corfdir, F. Feix, L. Geelhaar and H. Riechert, *Nano Lett.*, 2017, **17**, 1529.

24 X. Y. Feng, R. Li, M. L. Wang and Y. B. Chen, *J. Mater. Chem. A*, 2018, **6**, 11180.

25 M. G. Kibria, F. A. Chowdhury, S. Zhao, B. Alotaibi, M. L. Trudeau, H. Guo and Z. Mi, *Nat. Commun.*, 2015, **6**, 6797.

26 Y.-C. Lee, Y.-L. Chueh, C.-H. Hsieh, M.-T. Chang, L.-J. Chou, Z. L. Wang, Y.-W. Lan, C.-D. Chen, H. Kurata and S. Isoda, *Small*, 2007, **3**(8), 1356–1361.

27 J. Zhang and F.-X. Xiao, *J. Mater. Chem. A*, 2017, **5**, 23681.

28 X.-C. Dai, S. Hou, M.-H. Huang, Y.-B. Li, T. Li and F.-X. Xiao, *J. Phys. Energy*, 2019, **1**, 022002.

29 D. W. Flaherty, N. T. Hahn, R. A. May, S. P. Berglund, Y.-M. Lin, K. J. Stevenson, Z. Dohnalek, B. D. Kay and C. B. Mullins, *Acc. Chem. Res.*, 2012, **45**, 434.

30 Z. Dohnalek, G. A. Kimmel, D. E. McCready, J. S. Young, A. Dohnalkova, R. S. Smith and B. D. Kay, *J. Phys. Chem. B*, 2002, **106**, 3526.

31 D. W. Flaherty, Z. Dohnalek, A. Dohnalkova, B. W. Arey, D. E. McCready, N. Ponnusamy, C. B. Mullins and B. D. Kay, *J. Phys. Chem. C*, 2007, **111**, 4765.

32 D. W. Flaherty, D. Ferrer, T. R. Engstrom, P. L. Tanaka and C. B. Mullins, *J. Phys. Chem. C*, 2009, **113**, 12742.

33 N. T. Hahn, H. Ye, D. W. Flaherty, A. J. Bard and C. B. Mullins, *ACS Nano*, 2010, **4**, 1977.

34 N. T. Hahn and C. B. Mullins, *Chem. Mater.*, 2010, **22**, 6474.

35 S. P. Berglund, D. W. Flaherty, N. T. Hahn, A. J. Bard and C. B. Mullins, *J. Phys. Chem. C*, 2011, **115**, 3794.

36 C. G. Read, Y. Park and K.-S. Choi, *J. Phys. Chem. Lett.*, 2012, **3**, 1872.

37 Y. J. Jang, Y. B. Park, H. E. Kim, Y. H. Choi, S. H. Choi and J. S. Lee, *Chem. Mater.*, 2016, **28**, 6054.

38 Y. Hou, Z. Xu and S. Sun, *Angew. Chem.*, 2007, **119**, 6445.

39 T.-C. Chao, S. Sakthinathan, T.-W. Chiu and Y. Fu, *J. Ceram. Soc. Jpn.*, 2019, **127**, 498.

40 E. A. Fugate, S. Biswas, M. C. Clement, M. Kim, D. Kim, A. Asthagiri and L. R. Baker, *Nano Res.*, 2019, **12**, 2390.

41 H. Shan, X. Dong, X. Cheng, Y. Si, J. Yu and B. Ding, *Nanoscale*, 2019, **11**, 14844.

42 A. R. C. Bredar, M. D. Blanchet, R. B. Comes and B. H. Farnum, *ACS Appl. Energy Mater.*, 2019, **2**, 19.

43 C. Wang, Q. Li, F. Wang, G. Xia, R. Liu, D. Li, N. Li, J. S. Spendelow and G. Wu, *ACS Appl. Mater. Interfaces*, 2014, **6**, 1243.

44 K. Chen, S. Song, K. Li and D. Xue, *CrystEngComm*, 2013, **15**, 10367.

45 M. Yin, C.-K. Wu, Y. Lou, C. Burda, J. T. Koberstein, Y. Zhu and S. O'Brien, *J. Am. Chem. Soc.*, 2005, **127**, 9506–9511.

46 M. S. Prevot, X. A. Jeanbourquin, W. S. Bouree, F. Abdi, D. Friedrich, R. Krol, N. Guijarro, F. L. Formal and K. Sivula, *Chem. Mater.*, 2017, **29**, 4952.

47 F.-X. Jiang, D. Chen, G.-W. Zhou, Y.-N. Wang and X.-H. Xu, *Sci. Rep.*, 2018, **8**, 2417.

48 J.-C. Dupin, D. Gonbeau, P. Vinatier and A. Levasseur, *Phys. Chem. Chem. Phys.*, 2000, **2**, 1319.

49 W. S. Epling, G. B. Hoflund, J. F. Weaver, S. Tsubota and M. Haruta, *J. Phys. Chem.*, 1996, **100**, 9929.

50 H.-Y. Chen and J.-H. Wu, *Appl. Surf. Sci.*, 2012, **258**, 4844.

51 H.-Y. Chen and J.-H. Wu, *Thin Solid Films*, 2012, **520**, 5029.

52 K. P. Ong, K. Baj, P. Blaha and P. Wu, *Chem. Mater.*, 2007, **19**, 634.

53 M. S. Prevot, N. Guijarro and K. Sivula, *ChemSusChem*, 2015, **8**, 1359.

54 Y. Dai, J. Yu, C. Cheng, P. Tan and M. Ni, *J. Mater. Chem. A*, 2020, **8**, 6984.

55 P. Liao and E. A. Carter, *J. Appl. Phys.*, 2012, **112**, 013701.

56 X. Y. Meng, G. W. Qin, S. Li, X. H. Wen, Y. P. Ren, W. L. Pei and L. Zuo, *Appl. Phys. Lett.*, 2011, **98**, 112104.

57 A. G. Tamirat, J. Rick, A. A. Dubale, W.-N. Su and B.-J. Hwang, *Nanoscale Horiz.*, 2016, **1**, 243.

58 B. Ahmmad, K. Leonard, Md. S. Islam, J. Kurawaki, M. Muruganandham, T. Ohkubo and Y. Kuroda, *Adv. Powder Technol.*, 2013, **24**(1), 160–167.

59 T. P. Martin, R. Merlin, D. R. Huffman and M. Cardona, *Solid State Commun.*, 1977, **22**(9), 565–567.

60 A. B. Garg and R. Rao, *Crystals*, 2018, **8**(6), 255.

61 A. Annamalai, A. Subramanian, U. Kang, H. Park, S. H. Choi and J. S. Jang, *J. Phys. Chem. C*, 2015, **119**, 3810.